THE JOURNAL OF PHYSICAL CHEMISTRY A
A JOURNAL OF THE AMERICAN CHEMICAL SOCIETY

pubs.acs.org/JPCA
Article

URVAvis: A Graphical User Interface for the Visual Mechanistic Analysis of Chemical Reactions Based on the Unified Reaction Valley Approach

Kevin Fleming and Elfi Kraka*

Cite This: J. Phys. Chem. A 2026, 130, 5928−5939
Read Online

ABSTRACT: The Unified Reaction Valley Approach (URVA) enables the precise mechanistic analysis of chemical reactions through the detailed examination of the reaction path (RP) traced by the reaction complex (RC) on the potential energy surface. In this approach, the curvature of the RP is decomposed into curvature components tied to changes in the RC's internal coordinates during a given reaction (e.g., changes in bond lengths, bond angles, or dihedral angles). The RP curvature decomposition is then analyzed to identify the reaction's key mechanistic events. However, this curvature decomposition analysis involves a fragmented and often time-consuming computational workflow requiring multiple visualization software. To address this analysis limitation, the URVAvis graphical user interface is introduced herein. URVAvis enables the user to visualize the data necessary for the curvature decomposition analysis in a single, integrated platform, thereby streamlining this analysis workflow and enhancing the practical usability of URVA for mechanistic studies. The capabilities of URVAvis are demonstrated for an elementary step of the astrochemically relevant gas-phase reaction between acetonitrile (CH_3CN) and the carbon monochloride ion (CCl^+). Through the URVAvis-facilitated analysis of the elementary step's RP curvature decomposition, essential mechanistic events of the reaction are elucidated.

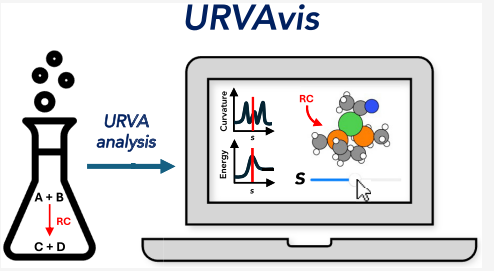

INTRODUCTION

Quantum chemistry has been widely employed since the 1980s for the theoretical investigation of chemical reaction mechanisms.[1,2] It continues to provide salient insights into a wide range of mechanisms, ranging from those of catalytic reactions with industrial applications[3−10] to those of astrochemical reactions occurring deep within outer space.[11−18] Such mechanistic insights emerge from the analysis of the potential energy surface (PES), which describes the potential energy of a given molecular system with respect to its geometrical configuration under the Born−Oppenheimer approximation.[19] Chemical reactions are characterized by the transformation of the reaction complex (RC), the union of the reacting species, into a product or set of products. This transformation occurs along the reaction pathway (RP) of the RC PES, and it often includes the formation of transition states (TS) and intermediate structures corresponding to stationary points on the PES. Thus, by mapping out the RP, the mechanism of the reaction can be predicted.

However, this mapping is far from trivial. For a given N-atom RC, its corresponding PES is a multidimensional surface with $N_{vib} = 3N - N_{tr}$ dimensions ($N_{tr} = 5$ or 6 for linear or nonlinear RCs, respectively). Hence, scanning this labyrinthine surface for a chemically meaningful RP is a formidable computational task. The intrinsic reaction coordinate (IRC) formalism of Fukui[20] is one of the most well-known methods to evaluate RPs, although other methods are also employed (e.g., the nudged elastic band (NEB)[21] and its doubly NEB (DNEB) variant,[22] the quadratic string method (QSM),[23] the zero- and finite-temperature string methods (SM),[24,25] and various growing string (GS) methods[26−28]). In recent years, machine learning (ML) techniques based on supervised learning[29−31] or reinforcement learning[32−34] have also been utilized to explore RC PESs.

Once the RP is mapped, the mechanistic changes to the RC during the reaction (e.g., bond formation/dissociation) can also be predicted. However, these changes are generally determined by considering only the stationary points along the RP, leading to an incomplete picture of the evolution of the RC between stationary points. Consequently, this stationary-point-centered approach limits the depth of mechanistic analysis for each reaction in a given reaction mechanism. To surpass this limitation and explore the evolution of the RC between stationary points, the Unified Reaction Valley Approach (URVA) can be utilized.[35] URVA focuses on an often-overlooked aspect of the RP during mechanistic studies: its *curvature*. Specifically, the RP is a curve in the multidimensional space of the RC PES, and its curvature varies as a function of the

Received: March 29, 2026
Revised: July 6, 2026
Accepted: July 7, 2026
Published: July 14, 2026

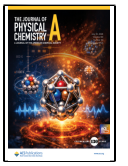

https://doi.org/10.1021/acs.jpca.6c02027
J. Phys. Chem. A 2026, 130, 5928−5939

reaction coordinate, the arc length of the RP, as shown in Figure 1. Examining this plot, one can identify segments of the reaction

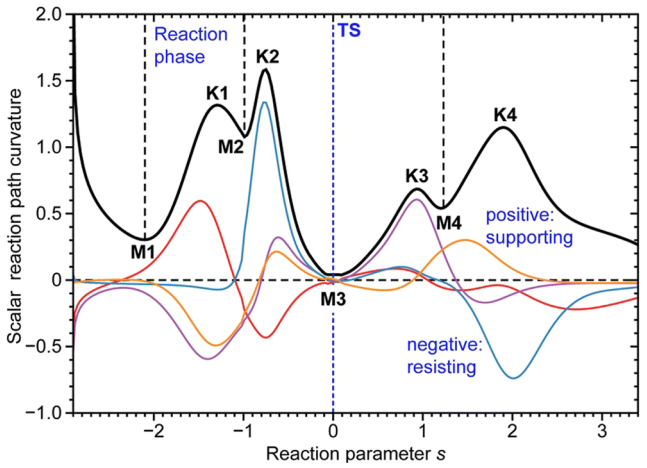

Figure 1. Example plot of the scalar RP curvature (solid black line) as a function of the reaction coordinate, *s*. TS denotes the transition state, K1−K4 indicate curvature maxima, and M1−M4 indicate curvature minima. An interval of the reaction coordinate containing a maximum flanked by two minima is called a reaction phase. Furthermore, the curvature can be decomposed into internal coordinate curvature components (solid colored lines). Reproduced from ref 35. with permission from the Royal Society of Chemistry.

coordinate containing a local curvature maximum flanked by two local curvature minima; each of these segments is referred to as a *reaction phase*, where one or more significant mechanistic changes to the RC occur, such as bond formation/dissociation.[36,37] Through the analysis of URVA reaction phases, such significant changes to the RC, which often occur at nonstationary points along the RP, are brought to light. URVA has been applied to a wide variety of reactions occurring in the gas phase, in solution, and even within enzymes − a comprehensive overview of these works is given in a previous review article.[35]

URVA analysis is a multistep process, and the mathematical formalism underpinning this process is reviewed in detail in previous literature.[38] To summarize, however, the first step involves computing the scalar curvature of each point along the RP − the RP is determined beforehand using the IRC formalism. For a given RP point specified by the reaction coordinate *s*, the scalar curvature is the magnitude of the curvature vector[38]

$$\boldsymbol{\kappa}(s) = \frac{-1}{\|\tilde{\mathbf{g}}(s)\|}(\tilde{\mathbf{f}}^{x}(s)\boldsymbol{\eta}(s) - [(\boldsymbol{\eta}(s))^{\dagger}\tilde{\mathbf{f}}^{x}(s)\boldsymbol{\eta}(s)]\boldsymbol{\eta}(s)) \quad (1)$$

where $\tilde{\mathbf{g}}(s)$ is the mass-weighted gradient vector, $\tilde{\mathbf{f}}^{x}(s)$ is the mass-weighted Hessian matrix, and $\boldsymbol{\eta}(s)$ is the RP direction vector, which can be expressed in terms of the mass-weighted gradient vector as[38]

$$\boldsymbol{\eta}(s) = -\frac{\tilde{\mathbf{g}}(s)}{\|\tilde{\mathbf{g}}(s)\|} \quad (2)$$

In the second step, the local curvature maxima and their flanking local minima are determined, leading to the identification of reaction phases.[36,37] Next, the curvature for each identified reaction phase is decomposed into smaller curvature components, corresponding to the changes of different portions of the RC during each phase.[38] These RC portions are described in terms of internal coordinates such as bond lengths, bond angles, and dihedral angles[38] or alternative coordinates such as Cremer-Pople puckering coordinates for cyclic RCs.[39] More specifically, for a set of N_{vib} internal coordinates, the curvature component associated with internal coordinate n ($n = 1, \cdots, N_{vib}$) is given by[38]

$$\kappa_n(s) = \mathbf{u}_n(s)^{\dagger}\boldsymbol{\kappa}(s) \quad (3)$$

where $\mathbf{u}_n(s)$ is the internal coordinate vector. The sign of $\kappa_n(s)$, in particular, is relevant to the curvature decomposition. When $\kappa_n(s)$ is positive, the associated internal coordinate undergoes a

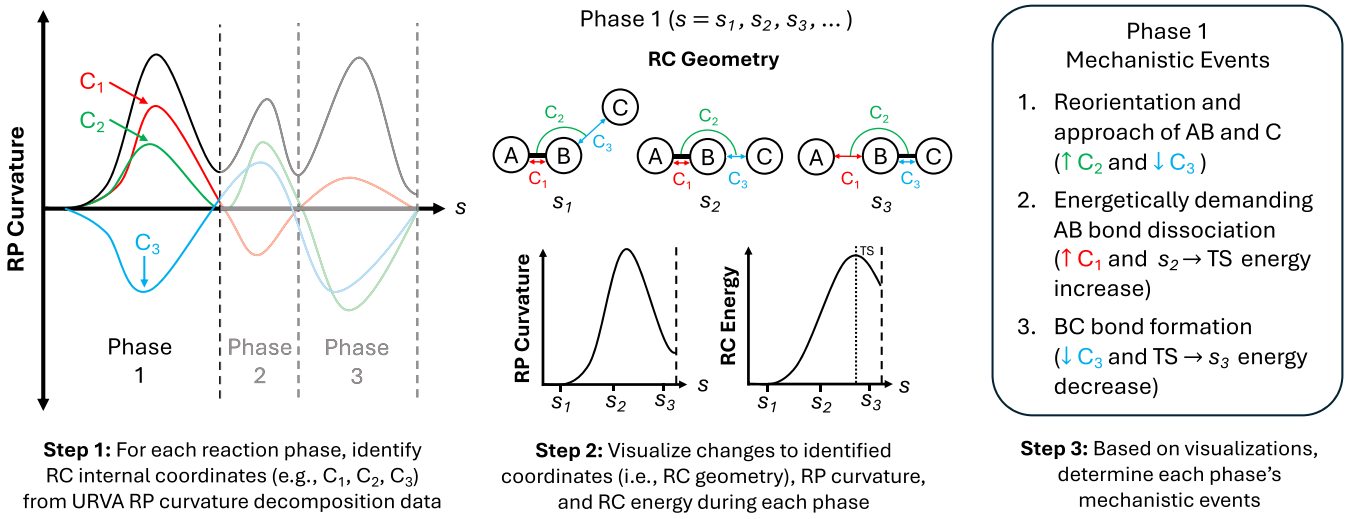

Figure 2. URVA RP curvature decomposition analysis for determining the mechanistic events of each URVA reaction phase. The analysis of a generic single replacement reaction AB + C → A + BC occurring during phase 1 of a multiphase elementary reaction is shown as an example. For the curvature and energy plots, dashed lines demarcate the end points of reaction phases along *s*. The *s* value of the transition state (TS) is indicated by the dotted line on the energy plot. See text for further explanation of each step.

https://doi.org/10.1021/acs.jpca.6c02027
J. Phys. Chem. A 2026, 130, 5928−5939

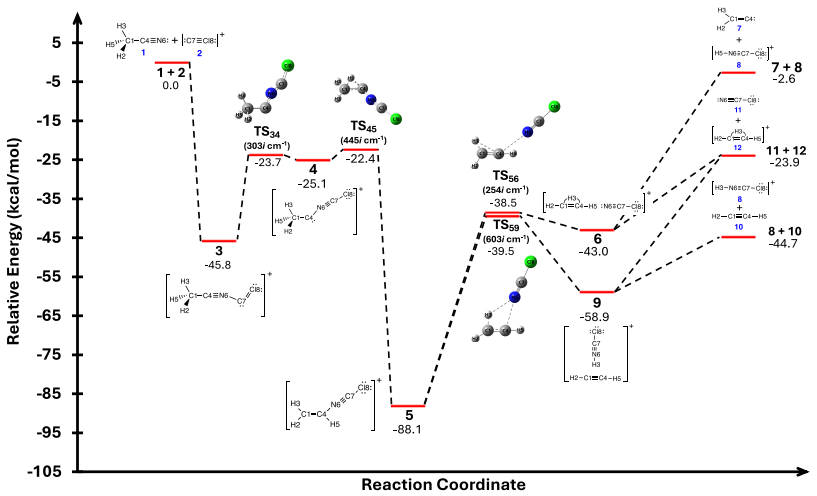

Figure 3. RC PES of the reaction between CH_3CN and CCl^+, evaluated at the DLPNO−CCSD(T)/aug-cc-pVTZ//MP2/cc-pVTZ level of theory. Singular imaginary frequencies of TS structures are also provided. Reproduced from ref 56. Copyright 2025 American Chemical Society.

change that contributes to (i.e., "supporting") the curving of the RP. Conversely, when $\kappa_n(s)$ is negative, the associated internal coordinate undergoes a change that is suppressing (i.e., "resisting") the curving of the RP. Since positive and negative curvature components both influence the curving of the RP, their associated internal coordinates are both of mechanistic significance. The $\kappa_n(s)$ values are plotted alongside the overall curvature (Figure 1), enabling the identification of mechanistically significant internal coordinates for each reaction phase.

While the curvature decomposition enables the identification of such internal coordinates, this identification is only the first step in a three-step URVA postprocessing analysis, referred to hereafter as *URVA RP curvature decomposition analysis*, for determining the mechanistic events for each reaction phase. The steps of this analysis are illustrated in Figure 2. Here, a generic single replacement reaction AB + C → A + BC, occurring during phase 1 of a multiphase elementary reaction, is considered as an example. In the first step of the analysis, the internal coordinates C_1 (AB bond length), C_2 (∠ABC bond angle), and C_3 (BC interatomic distance) can be identified as mechanistically significant internal coordinates for phase 1, since they have pronounced curvature component curves. To understand how changes to these internal coordinates during phase 1 are connected to the phase's mechanistic events, the second step of the analysis comes into play: simultaneously visualizing the changes to the RC geometry (described in part or in whole by the identified coordinates), the RC electronic energy, and RP curvature as a function of s. Other RC scalar properties besides electronic energy could also be visualized for this step (e.g., atomic charges) if desired; for simplicity, however, this additional analysis will not be conducted here. Visualizations of the energy and curvature are shown as plots of the two quantities as a function of s. The curvature plot enables the identification of the interval of s describing phase 1, which contains a local curvature maximum flanked by two local curvature minima. At several points within this identified interval (e.g., $s = s_1, s_2, s_3, \cdots$), the RC geometry can be visualized to assess the changes to its internal coordinates during this phase. Comparing the internal coordinates of the RC geometries at $s = s_1$, s_2, and s_3, there is an observed increase in C_1, increase in C_2, and decrease in C_3. For the third and final step of the analysis, these visualized changes to the three internal coordinates can be considered alongside the RC energy plot to determine the phase's mechanistic events. Through this step, three key mechanistic events for the AB + C → A + BC reaction are determined: the mutual approach and reorientation of the RC fragments AB and C (increase in C_2 and decrease in C_3), the energetically demanding dissociation of the AB bond (increase in C_1 and sharp increase in RC energy from s_2 to the TS), and finally the formation of the BC bond (decrease in C_3 and decrease in RC energy from the TS to s_3). This example reaction, albeit a simple one, demonstrates how URVA RP curvature decomposition analysis can yield mechanistic insights for each URVA reaction phase.

However, there is a serious practical challenge that arises when attempting to conduct URVA RP curvature decomposition analysis: the simultaneous visualization of the RC geometry, RP curvature, and RC energy as a function of the reaction coordinate (Figure 2, Step 2). Previously, multiple molecular and data visualization software were required for this step of this analysis, thereby making it a fragmented and often time-consuming endeavor. To circumvent this bottleneck during URVA RP curvature decomposition analysis, URVAvis is introduced herein. URVAvis is a graphical user interface (GUI) that interactively and simultaneously visualizes the evolution of a given reaction's RP curvature, RC geometry, and RC electronic energy. By eliminating the need for multiple visualization software, this GUI greatly streamlines URVA RP curvature decomposition analysis. Thus, URVAvis can be utilized for the visual mechanistic analysis of chemical reactions based on URVA. URVAvis is open source and free of charge; it is publicly available through the URVAvis GitHub repository,[40] where the documentation can also be found. In this work, a detailed description of the program and its role in facilitating URVA RP curvature decomposition analysis is given.

METHODS

Technical details pertaining to URVAvis (i.e., code development, key libraries utilized, compatibility requirements, and licensing) can be found in Section S1 of the Supporting Information. To demonstrate the capabilities of URVAvis, an elementary step of the gas-phase reaction between acetonitrile (CH_3CN) and the carbon monochloride ion (CCl^+) will be considered in this work.

https://doi.org/10.1021/acs.jpca.6c02027
J. Phys. Chem. A 2026, 130, 5928−5939

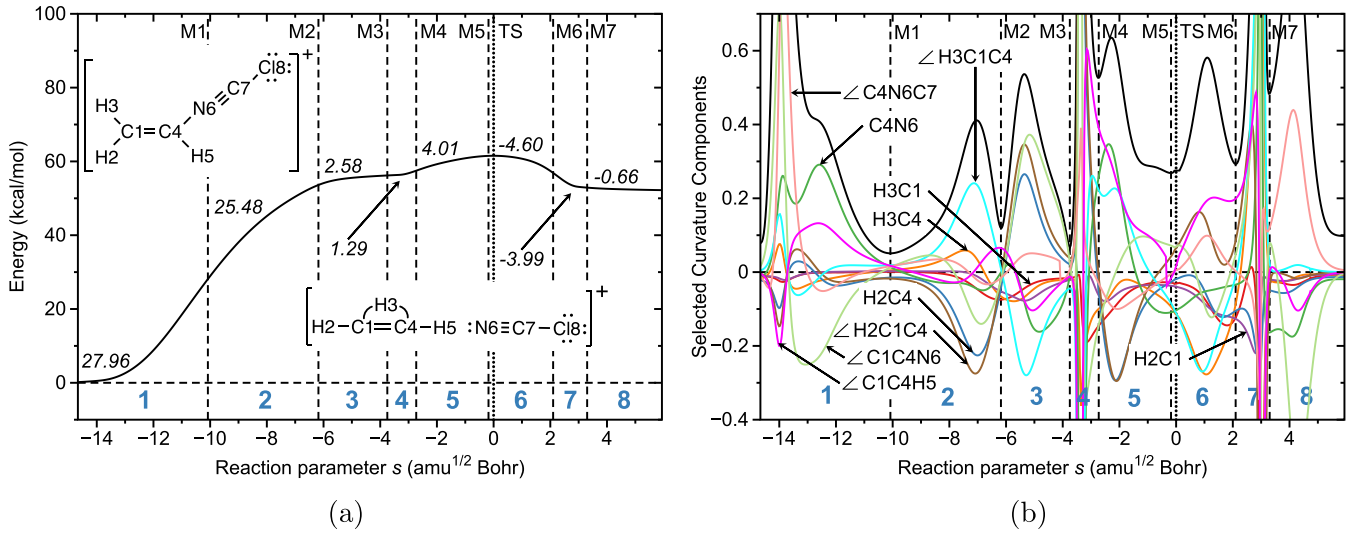

Figure 4. RC evolution during the eight-phase reaction of **5** to form **6**, as illustrated by the (a) reaction energy profile, including the RC energy change for each phase, and the (b) total RP curvature (solid black line) and the decomposition into curvature components (colored solid lines). The TS is indicated by the black dotted line shown at $s = 0$ amu$^{1/2}$ Bohr, while the curvature minima separating each reaction phase are denoted by black dotted lines labeled M1-M7. Reproduced from ref 56. Copyright 2025 American Chemical Society.

The $CH_3CN + CCl^+$ Reaction

CH_3CN was first detected in interstellar molecular clouds Sgr A and B2 in 1971[41] and has since been detected in various astronomical systems ranging from comets[42−44] to protoplanetary disks.[45,46] Unlike acetonitrile, however, CCl^+ has not been detected in outer space yet, although it may be present in the $z = 0.89$ molecular absorber toward the quasar PKS 1830−211, where HCl, its proposed chemical precursor,[47] and CF^+, its fluorinated counterpart,[48] were previously detected. CH_3CN has also been detected in this molecular absorber as well,[49] suggesting that CH_3CN and CCl^+—if present—may react therein. In 2021, Krohn et al.[50] experimentally investigated this reaction, observing the formation of NCCl, $HNCCl^+$, C_2H_2, and $C_2H_3^+$ as the primary products. The C_2H_2 product, in particular, is of special astrochemical significance. C_2H_2 has been extensively investigated for its potential role as a chemical precursor to the formation of complex organic molecules (COMs)[51,52] that serve as the building blocks of prebiotic molecules, such as amino acids.[53] The exogenous hypothesis of the origin of life on Earth contends that these prebiotic molecules were delivered to a primordial Earth through astronomical objects that incorporated these materials during their formation (e.g., comets, meteoroids, and asteroids), thereby providing the starting materials necessary for life to emerge.[54,55] Thus, the $CH_3CN + CCl^+$ reaction may have acted as one synthetic starting point for the formation of COMs and subsequently prebiotic molecules in outer space − molecules that may have enabled the origin of life on Earth.

Mechanistic Analysis

Recently, we mechanistically examined this reaction.[56] The RC PES (Figure 3) shows the conversion of CH_3CN (**1**) and CCl^+ (**2**) into products **7**,**8**, and **10**−**12**, which are the same products experimentally observed by Krohn et al.[50] All single point energies for the stationary point structures were evaluated at the DLPNO−CCSD(T)[57]/aug-cc-pVTZ[58,59]//MP2[60]/cc-pVTZ[59,61] level of theory, corrected for zero-point vibrational energies evaluated from frequency calculations at the MP2/cc-pVTZ level of theory.[56] Initially, **1** and **2** react in a barrierless reaction to form intermediate **3**, which then endothermally isomerizes to form the highly unstable carbene intermediate **4**. This carbene then undergoes a highly exothermic hydrogen migration reaction to form **5**, the most stable intermediate in the PES. This intermediate can traverse four different paths on the PES to form the aforementioned products.

Prior to product formation, however, intermediate **5** can transform into intermediate **6**. This elementary reaction merits further examination. Comparing only the stationary point geometries of **5**, **6**, and transition state $\mathbf{TS}_{56}$, it may appear that the only mechanistically significant events occurring during the reaction are the cleavage of **5**'s C4N6 bond and the formation of a 3-center, 2-electron (3c-2e) bond between H3, C1, and C4. However, there are other significant mechanistic events that are not accounted for by this simple comparison. To determine these events, we applied URVA to this reaction.[56]

The URVA results for the reaction are shown in Figure 4.[56] Figure 4a,4b depicts the reaction energy profile with labeled reaction phases and the RP curvature with curvature components, respectively. There are eight reaction phases along the reaction coordinate s, and each reaction phase contains a curvature local maximum with two adjacent curvature minima. Through URVA RP curvature decomposition analysis, the mechanistic events of each phase were determined.[56] The RC structural changes across the eight phases are shown in Figure 5; in addition, a phase-by-phase animation of the reaction ("urva_reaction_phases.mp4") is given in the Supporting Information. To facilitate the discussion in the following section, a brief overview of the chemical insights for each phase will be provided.

Phases 1 and 2 describe the cleavage of the C4N6 single bond to form $C_2H_3^+$ and NCCl fragments bound together to form a van der Waals (VdW) complex. During phase 3, H2 forms a 3c-2e bond with C1 and C4, as depicted in Figure 5; this isomer of $C_2H_3^+$, which contains a bridged hydrogen atom bonded to both C1 and C4, will be referred to hereafter as B−$C_2H_3^+$. In addition, both the $C_2H_3^+$ and NCCl fragments begin to undergo reconfiguration—that is, they begin to mutually distance themselves from each another and undergo reorientation (i.e., toward the collinear arrangement of intermediate **6**). In phase 4,

https://doi.org/10.1021/acs.jpca.6c02027
J. Phys. Chem. A 2026, 130, 5928−5939

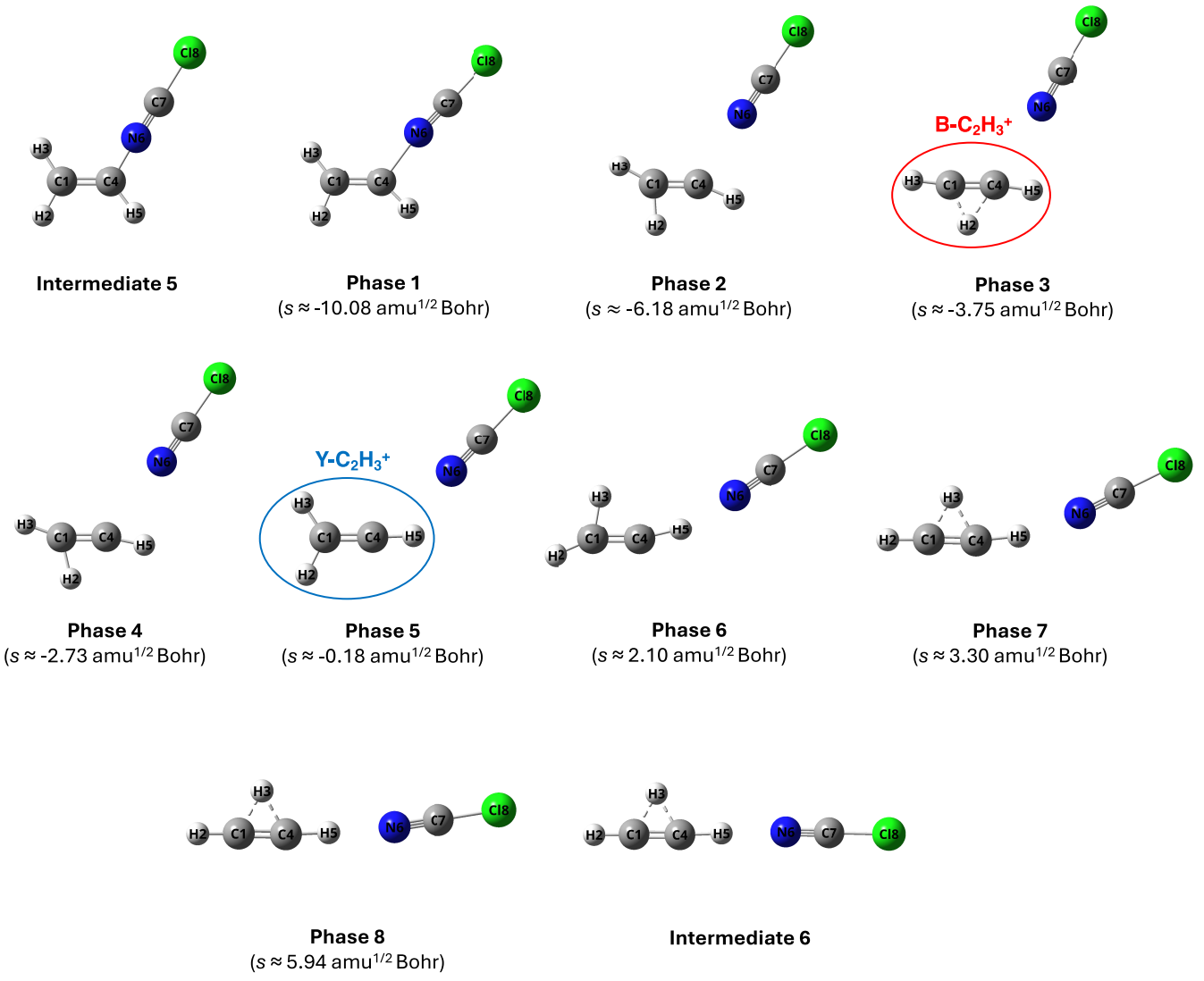

Figure 5. RC geometry changes during the eight-phase reaction of **5** to form **6**. The RC geometry at the end of each phase is shown, with the reaction coordinate (s) values corresponding to those shown in Figure 4. An example of each $C_2H_3^+$ isomer (i.e., B−$C_2H_3^+$ and Y−$C_2H_3^+$) is circled.

the 3c-2e bond of B−$C_2H_3^+$ undergoes dissociation and H2 is once again singly bonded to C1. Figure 4a shows a sudden increase in the RC energy—by ∼5 kcal/mol—during phases 4 and 5 that reaches an energy maximum when transition state $\mathbf{TS}_{56}$ is formed near the very beginning of phase 6. This anomalous increase in the energy shortly prior to TS formation can be explained by the conversion of B−$C_2H_3^+$ into a Y-shaped isomer of $C_2H_3^+$ during phases 4 and 5 (Figure 5) − this isomer will be referred to hereafter as Y−$C_2H_3^+$. Previous theoretical[62−67] and experimental[68−71] studies have demonstrated that B−$C_2H_3^+$ is more energetically stable than Y−$C_2H_3^+$ by $\gtrsim$4 kcal/mol; thus, the conversion of the former to the latter during phases 4 and 5 results in the sudden increase in the RC energy. During phases 6 and 7, however, Y−$C_2H_3^+$ converts back into B−$C_2H_3^+$, resulting in a RC energy decrease that plateaus near the end of phase 7 once the new B−$C_2H_3^+$ isomer is fully formed. Considered together, phases 4−7 describe the conversion of B−$C_2H_3^+$to Y−$C_2H_3^+$ and back; this series of transformations explains the soft bump in the RC energy from phases 4−7. Finally, during phase 8, the B−$C_2H_3^+$ and NCCl fragments undergo further mutual distancing and reorientation, eventually resulting in the formation of intermediate **6** after phase 8. There is no reaction phase to mark the termination of fragment reorientation due to numerical instabilities that were encountered by URVA when evaluating the curvature of the reaction's exit channel; however, no other mechanistic events occur beyond phase 8.

This URVA-based description of the elementary reaction provides a significantly more precise mechanistic description than what could be gleaned from only comparing stationary point structures on the PES. A mere comparison of the stationary point geometries of **5**, **6**, and $\mathbf{TS}_{56}$ would give the false impression that the only mechanistically significant events occurring during the reaction would be the cleavage of the C4N6 bond and the formation of the 3c-2e bond between H3, C1, and C4. However, this simple mechanistic description cannot explain the soft bump in the RC energy near the TS. Our analysis of the URVA data for this reaction addressed this energetic anomaly by revealing that there are also intermediary transformations between the B−$C_2H_3^+$ and Y−$C_2H_3^+$ isomers of the RC's $C_2H_3^+$ fragment.[56] These transient yet significant mechanistic events, reflecting the exceptional mobility of the hydrogen atoms of the $C_2H_3^+$ RC fragment during the reaction,

https://doi.org/10.1021/acs.jpca.6c02027
J. Phys. Chem. A 2026, 130, 5928−5939

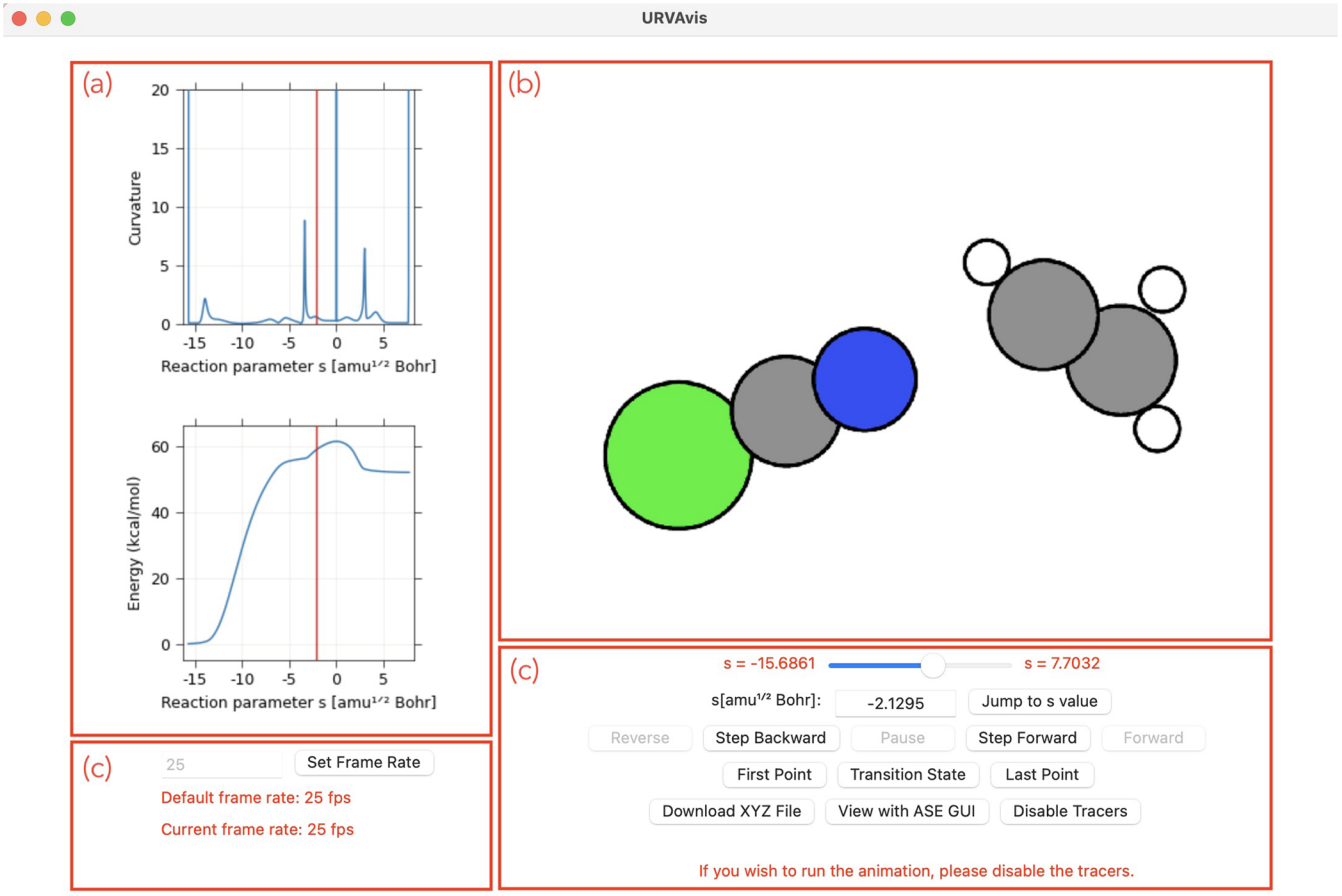

Figure 6. URVAvis GUI, with the (a) curvature and energy plots, (b) 2D RC visual, and (c) RC visual control panel. The elementary reaction being analyzed is the conversion of intermediate **5** to intermediate **6** (see Figure 3). Note: The frame rate controls on the bottom-left side of the GUI are part of the RC visual control panel. Atoms are labeled as follows: white for hydrogen, blue for nitrogen, gray for carbon, and green for chlorine.

are captured by the eight URVA phases, thus explaining the anomalous shape of the reaction's energy profile.

Importantly, the mechanistic events for each of the reaction's eight URVA reaction phases were determined through URVA RP curvature decomposition analysis.[56] In the following section, URVAvis will be applied to the reaction to first describe the program's functionalities and then demonstrate how the program can facilitate the URVA RP curvature decomposition analysis of any given reaction phase.

RESULTS AND DISCUSSION

URVAvis Input Files

To explain the functionalities of URVAvis, the required input files will be described first. There are three input files:

1. **RC geometry file**: Contains the geometry of the RC at each point along the RP in the XYZ chemical file format.
2. **RC energy file**: Contains the electronic energy of the RC at each point along the RP in the CSV file format.
3. **RP curvature file**: Contains the scalar curvature at each point along the RP in the DAT file format.

The URVA2025 program,[72] developed to conduct URVA analysis, automatically generates the RC energy file and the RP curvature file as output. To generate the RC geometry file, our group has developed a separate postprocessing script that reads in the output file of a preceding IRC calculation and extracts all calculated geometries contained within it. This script, along with the URVA2025 program, can currently be obtained upon request, although both will be made publicly available in the near future on our group's GitHub page,[73] with all documentation pertaining to installation and usage included. To facilitate the URVA calculation, the preceding IRC calculation implements the reaction path following procedure of Hratchian and Kraka,[74] which can be utilized to track the RP far out into its entrance and exit channels.

URVAvis Functionalities

An example of the application of URVAvis is shown in Figure 6. Here, the conversion of intermediate **5** to intermediate **6** during the reaction between CH_3CN and CCl^+ (Figure 3) is examined. An animation of URVAvis being applied to this particular elementary reaction can be found on the URVAvis GitHub page.[40] The GUI has three prominent features: the 2D RC visual, the RC visual control panel, and the curvature and energy plots.

2D Visual of RC. Based on the geometries contained in the RC geometry input file, the program generates a 2D animation frame for each point along the reaction path (Figure 6b). For a specified reaction coordinate s, its corresponding frame is shown in the GUI. The Atomic Simulation Environment (ASE) Python library[75,76] is utilized by the program to automatically generate these frames; the process by which URVAvis chooses the optimal animation plane for the RC visual is described in Section S2 of the Supporting Information. This is a one-time process and takes only a few minutes to complete, depending on the number of geometries to be processed. Once generated, the frames are

https://doi.org/10.1021/acs.jpca.6c02027
J. Phys. Chem. A 2026, 130, 5928−5939

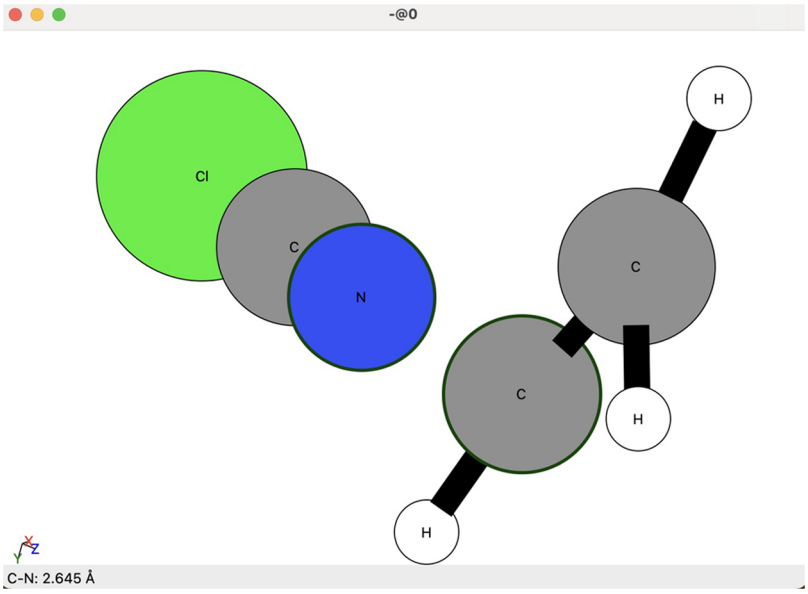

Figure 7. ASE GUI[75,76] integrated into URVAvis. The RC geometry depicted is the same as that of Figure 6 but presented from a 3D perspective. The user can rotate the RC in 3D space, render the RC in the default format (e.g., Figure 6) or the ball-and-stick format depicted here, and view internal coordinate values. An example of the GUI being used to evaluate the interatomic distance between carbon and nitrogen atoms (circled in dark green) is shown, with the CN interatomic distance printed at the bottom-left corner of the GUI.

stored in a new subdirectory within the same directory as the input files, and the frames can be reused if the program is rerun at a later time.

RC Visual Control Panel. This panel, shown right below the visual of the RC (Figure 6c), contains a set of controls that the user can use to visually examine the changes to the RC and its properties during its reaction. At the top of the panel is a slider that can be manually controlled by one's mouse cursor. The user can move the slider forward or backward along s.

There are four additional ways for the user to explore the reaction coordinate as well. For the first option, the user can enter a specific value of s they would like to examine in the text field below the slider and press the "Jump to s value" button. For the second option, there is a series of buttons below this text field that can be used to animate the reaction in either direction (i.e., "Reverse", "Pause", and "Forward"). The frame rate of the animations, which is 25 frames per second by default, can be adjusted by the user using the controls on the bottom left-hand side of the interface; the user can enter the new frame rate into the frame rate text field and press the "Set Frame Rate" button. Third, the user can simply move from one value of s to its neighboring value (i.e., "Step Forward" and "Step Backward") Lastly, below the animation controls, there is a series of buttons which can instantly shift the slider to the first point along the RP (i.e., "First Point"), the transition state corresponding to $s = 0.00$ amu$^{1/2}$ Bohr (i.e., "Transition State"), or the last point along the RP (i.e., "Last Point").

If the user would like to obtain the geometry of the RC at a particular value of s for further quantum chemical analysis (e.g., Natural Bond Orbital (NBO) analysis[77,78] or the Quantum Theory of Atoms and Molecules (QTAIM)[79]), they can press the "Download XYZ File" button, which will write an XYZ file containing the RC's geometry to the same directory as the URVAvis input files. Alternatively, the "View with ASE GUI" will generate a new window with a 3D visual of the RC at s (Figure 7). This 3D structure is generated by the ASE GUI,[75,76] integrated into URVAvis, which allows the user to rotate the structure in 3D space, and evaluate the values of specific internal coordinates, and render the RC in ball-and-stick or the default format shown in Figure 6, among other functions.[75,76] As demonstrated later, the ASE GUI is especially useful during the URVA RP curvature decomposition analysis of a given reaction phase.

Curvature and Energy Plots. On the left side of the GUI (Figure 6a), there are two interactive plots that describe the RP scalar curvature and RC energy as a function of reaction coordinate s. These plots can be cross-compared with the evolving 2D visual of the RC to analyze the URVA RP curvature decomposition, given in plots such as Figure 4b, and thus determine the phase's key mechanistic events. In addition, the plots contain tracers, red vertical lines that correspond to the value of s specified by the user through the RC visual control panel; these plot tracers make the comparison between the plots and the RC visual easier. If the user changes the value of s, the tracers will shift to the new value of s accordingly.

Currently, the tracers cannot be used when the reaction is being automatically animated by the GUI. This measure is taken to prevent the program from crashing, especially at higher frame rates. To ensure that the user does not accidentally use the tracers when animating the reaction, the animation buttons are automatically disabled when the tracers are enabled, as shown in Figure 6c. If the user would like to enable the animation buttons, they can simply press the "Disable Tracers" button on the bottom right-side of the visual control panel. After the tracers are disabled, they can always be re-enabled by pressing the "Enable Tracers" button, which appears after the tracers have been disabled. However, there is no risk of crashing if the user moves the slider with their mouse while the tracers are enabled — a suitable alternative to the automatic animation option if the user encounters any issues.

URVA RP Curvature Decomposition Analysis with URVAvis

As previously mentioned, URVAvis can be utilized by the user to facilitate the URVA RP curvature decomposition for each reaction phase and thus determine the phases' key mechanistic

https://doi.org/10.1021/acs.jpca.6c02027
J. Phys. Chem. A 2026, 130, 5928−5939

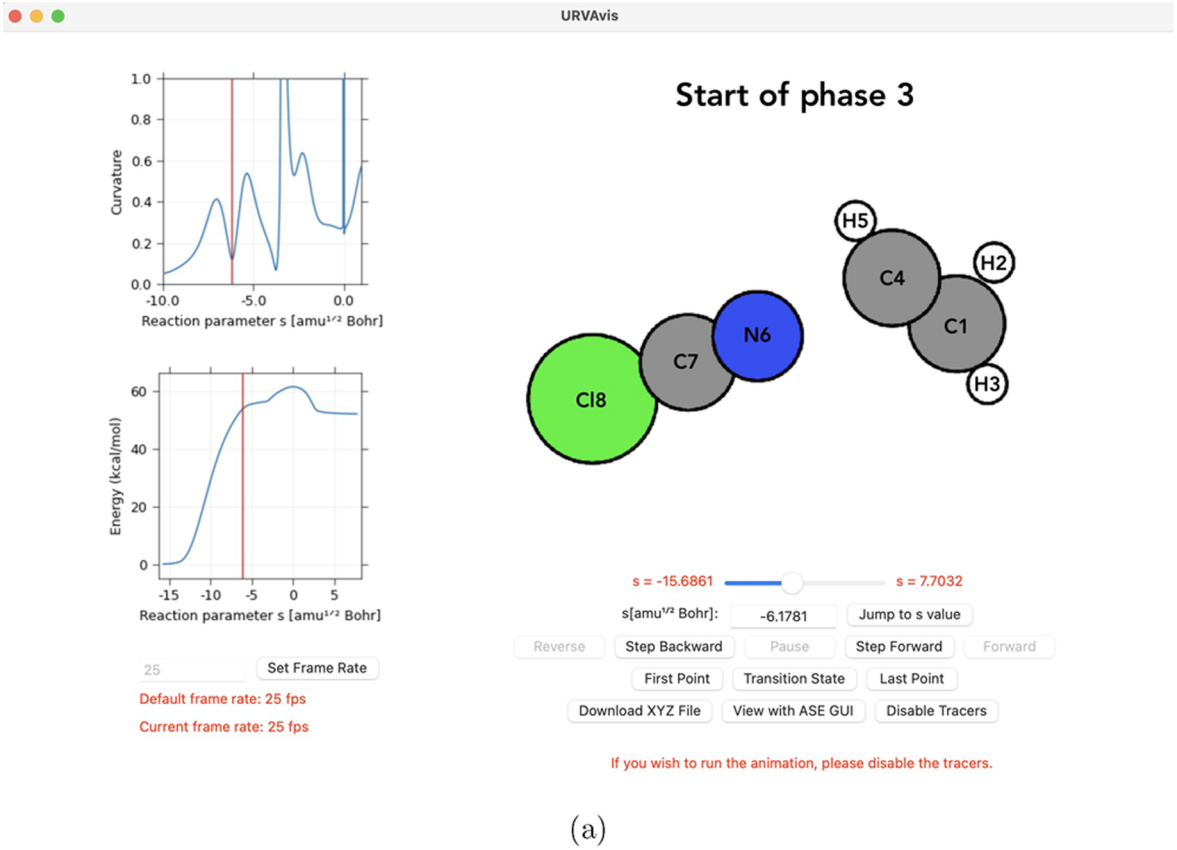

(a)

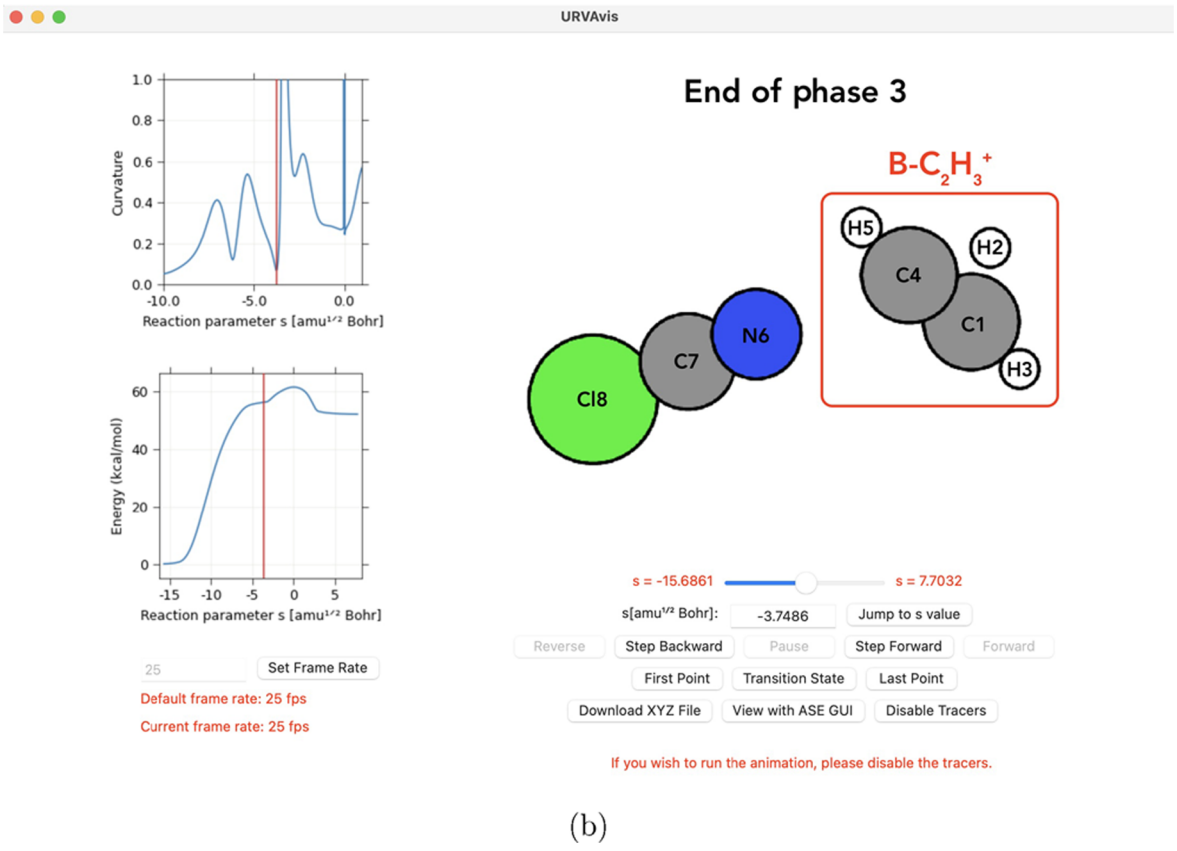

(b)

Figure 8. URVA reaction phase 3, viewed with the URVAvis GUI. The curvature, energy, and geometry at the (a) start and (b) end of the phase are depicted. Labels for the atoms, the start/end of the phase, and the B−$C_2H_3^+$ fragment are added.

https://doi.org/10.1021/acs.jpca.6c02027
J. Phys. Chem. A 2026, 130, 5928−5939

event(s). To demonstrate this capability, URVAvis will be utilized in this section to analyze the RP curvature decomposition of URVA reaction phase 3 (Figure 4). Through this analysis, two essential mechanistic events of the reaction from **5** to **6** will be unraveled.

For the first step of the URVA RP decomposition analysis (Figure 2), the internal coordinates whose pronounced curvature components make up the phase 3 curvature decomposition are identified. As shown in Figure 4b, the phase 3 curvature decomposition involves many curvature components, but the five most pronounced curvature component curves correspond to the internal coordinates H2C4, C4N6, ∠H2C1C4, ∠C1C4N6, and ∠H3C1C4.

With these five internal coordinates in mind, we can utilize URVAvis for the second step of the analysis: the visualization of the changes to the internal coordinates (i.e., RC geometry), RP curvature, and RC energy during phase 3. Figure 8a,8b depict two static snapshots of URVAvis at the start and end of the phase, respectively, as indicated by the local curvature minima marked by the GUI's red curvature plot tracer. In addition, an animation of phase 3 being navigated with URVAvis ("urva-vis_phase-3.mp4") is given in the Supporting Information. Examining the two snapshots and the animation, it becomes visibly evident that the H2C4, C4N6, ∠H2C1C4, ∠C1C4N6, and ∠H3C1C4 internal coordinates do indeed change to various degrees. These changes can be more precisely quantified using the aforementioned ASE GUI integrated into URVAvis (Figure 7). Using the ASE GUI, we find that during phase 3, there is a decrease in the H2C4 (1.6 Å to 1.4 Å) and ∠H2C1C4 (86.2° to 67.2°) coordinates, accompanied by an increase in the C4N6 (2.3 Å to 2.6 Å), ∠H3C1C4 (152.4° to 173.1°), and ∠C1C4N6 (121.2° to 121.7°) coordinates. Finally, evaluating the changes in the RC energy profile, we observe that the RC energy, which sharply increased in the preceding phases 1 and 2 due to the energetic cleavage of the C4N6 bond, nearly plateaus during phase 3 (i.e., the energy increases only slightly—on the order of a few kcal/mol).

Equipped with these geometric and energetic observations, we reach the third and final step of the analysis: determining the mechanistic events. The observations reveal the two key mechanistic events occurring during the phase. The first, most apparent mechanistic event is the reorientation of the $C_2H_3^+$ fragment's hydrogen atoms H2 and H3 to form the B−$C_2H_3^+$ isomer shown in Figure 8b, a process that is described by the changes to the H2C4, ∠H2C1C4, and ∠H3C1C4 coordinates. As shown in the phase 3 URVAvis animation, this reorientation process involves the rotation of H2 toward C4 to form a 3c-2e bond with C1 and C4, resulting in the reduction of the H2C4 and ∠H2C1C4 coordinates, while H3 becomes increasingly aligned with the C1C4 bond axis, resulting in the ∠H3C1C4 coordinate approaching 180°. In our previous work,[56] we applied NBO analysis to the RC geometry at the end of phase 3 and verified that 3c-2e bond formation does indeed occur; with URVAvis, this RC geometry—or any other geometry along *s*—can now be directly exported from the GUI for such an analysis. The first mechanistic event, however, explains neither the changes to the C4N6 and ∠C1C4N6 coordinates nor the slight increase in the energy during phase 3. Rather, these particular changes can be described by the second mechanistic event: the initial reconfiguration (i.e., the mutual distancing and reorientation) of the NCCl and $C_2H_3^+$ fragments, formed after C4N6 bond cleavage during phases 1 and 2. More specifically, as shown in the animation, the mutual distancing between the two fragments involves an increase in the C4N6 coordinate while the fragment reorientation involves a very slight increase in the ∠C1C4N6 coordinate. Although the mutual distancing and fragment reorientation processes are seemingly trivial compared the formation of B−$C_2H_3^+$, these two processes continue for the remainder of the elementary reaction, as evidenced by the structural changes to the RC during phases 4−8 (Figure 5) − ultimately resulting in the distanced, collinear configuration of the NCCl and $C_2H_3^+$ fragments by the end of the reaction.

From an energetics standpoint, the initial mutual distancing and fragment reorientation explain the slight increase in energy during phase 3. Since NCCl has a high dipole moment of ∼2.8 D[80,81] and the B−$C_2H_3^+$ fragment is both charged and has a moderate dipole moment of ∼1.1 D,[62] the mutual distancing and fragment reorientation processes requires energy to overcome the attractive ion-dipole and dipole−dipole interactions between the two fragments. This energetic penalty may be mitigated by the energy released during the formation of the B−$C_2H_3^+$ fragment's 3c-2e bond, but further analysis beyond the scope of the present work would be needed to quantitatively assess this energetic counterbalancing between the two mechanistic events.

Overall, the URVAvis-facilitated analysis of the phase 3 curvature decomposition elucidate the phase's two key mechanistic events, thus providing a detailed mechanistic description of this phase that also qualitatively accounts for the phase's near-plateauing of the RC energy profile. As mentioned in the beginning of this section, these two mechanistic events are also essential to the **5** to **6** reaction: the formation of the B−$C_2H_3^+$ fragment during phase 3 sets the stage for the aforementioned chemical conversions between B−$C_2H_3^+$ and Y−$C_2H_3^+$ during phases 4−7, while the initial reconfiguration of the RC fragments kicks off a continual reconfiguration of the fragments that continues until the very end of the reaction. Without URVAvis, acquiring these mechanistic insights from the URVA RP curvature decomposition analysis is time-consuming and fragmented due to the need for multiple software to simultaneously visualize the curvature, energy, and geometry as a function of the reaction coordinate. With URVAvis, however, this multifaceted analysis is conducted on a single, integrated software platform, making it significantly more straightforward and streamlined than before.

CONCLUSIONS

URVAvis, a GUI for the visual mechanistic analysis of chemical reactions based on URVA, is presented in this work. Designed to streamline the URVA RP curvature decomposition analysis of output data generated by the URVA2025[72] program, the GUI eliminates the need for utilizing multiple molecular and data visualization software when analyzing the curvature decomposition of each URVA reaction phase. The program's interactive and simultaneous visualization of the RP curvature, RC energy, and RC geometry as a function of the reaction coordinate provides a simplified, user-friendly approach to studying reaction phases. This simplification, in turn, enables the user to more easily determine the mechanistic events of each phase, thus facilitating mechanistic studies of reactions with URVA.

In future versions of URVAvis, two new sets of GUI features will be included. The first of these will be plots presenting the changes in various nonenergetic scalar RC properties as a function of the reaction coordinate (e.g., internal coordinate values, atomic charges derived from NBO analysis,[77,78] dipole

https://doi.org/10.1021/acs.jpca.6c02027
J. Phys. Chem. A 2026, 130, 5928−5939

moments, etc.). Including plots of these properties alongside the current URVAvis energy and curvature plots will enable the user to acquire even more detailed insights into the mechanistic events revealed through the URVA RP curvature decomposition analysis. The second set of features to be added to URVAvis pertain to the GUI's energy and curvature plots. These plots, in contrast to their counterparts in Figure 4, currently do not include lines demarcating reaction phases and, in the case of the curvature plot, do not include the curvature component curves either. However, these features will be included in future GUI updates. Once reaction phase demarcation lines for both plots and curvature decomposition curves for the curvature plot are included, the plots will resemble the Figure 4 plots. Hence, these additions would expand the utility of URVAvis beyond facilitating URVA RP curvature decomposition analysis and allow the user to also easily generate energy and curvature plots that could be readily disseminated to the research community (e.g., through presentations or publications).

■ ASSOCIATED CONTENT

Supporting Information

The Supporting Information is available free of charge at https://pubs.acs.org/doi/10.1021/acs.jpca.6c02027.

URVAvis technical details and a description of the process for selecting the optimal animation plane for the URVAvis 2D RC visual (PDF)

urva_reaction_phases.mp4: A descriptive, phase-by-phase animation of the eight URVA reaction phases describing the reaction from intermediates **5** to **6** (MP4)

urva-vis_phase-3.mp4: An animation of the user examining URVA reaction phase 3 of the reaction from intermediates **5** to **6** with URVAvis (MP4)

■ AUTHOR INFORMATION

Corresponding Author

Elfi Kraka − *Computational and Theoretical Chemistry Group (CATCO), Department of Chemistry, Southern Methodist University, Dallas, Texas 75275-0314, United States;* orcid.org/0000-0002-9658-5626; Email: ekraka@mail.smu.edu

Author

Kevin Fleming − *Computational and Theoretical Chemistry Group (CATCO), Department of Chemistry, Southern Methodist University, Dallas, Texas 75275-0314, United States*

Complete contact information is available at: https://pubs.acs.org/10.1021/acs.jpca.6c02027

Notes

The authors declare no competing financial interest.

■ ACKNOWLEDGMENTS

The authors thank Dr. Thomas M. Sexton for his valuable suggestions, as well as the SMU O'Donnell Data Science and Computing Center for providing excellent computational resources. K.F. thanks the SMU Moody School of Graduate and Advanced Studies for their support through the SMU Moody Graduate Fellowship and the NASA Texas Space Grant Consortium (TSGC) for their support through the NASA TSGC Graduate Fellowship.

■ REFERENCES

(1) Eksterowicz, J. E.; Houk, K. Transition-State Modeling With Empirical Force Fields. *Chem. Rev.* **1993**, *93*, 2439−2461.

(2) Hayashi, H.; Maeda, S.; Mita, T. Quantum Chemical Calculations for Reaction Prediction in the Development of Synthetic Methodologies. *Chem. Sci.* **2023**, *14*, 11601−11616.

(3) Hosseini, H.; Herring, C. J.; Nwaokorie, C. F.; Sulley, G. A.; Montemore, M. M. Computational Design of Catalysts with Experimental Validation: Recent Successes, Effective Strategies, and Pitfalls. *J. Phys. Chem. C* **2024**, *128*, 18144−18157.

(4) Houk, K. N.; Cheong, P. H.-Y. Computational Prediction of Small-Molecule Catalysts. *Nature* **2008**, *455*, 309−313.

(5) Lam, Y.-h.; Grayson, M. N.; Holland, M. C.; Simon, A.; Houk, K. Theory and Modeling of Asymmetric Catalytic Reactions. *Acc. Chem. Res.* **2016**, *49*, 750−762.

(6) Peng, Q.; Paton, R. S. Catalytic Control in Cyclizations: From Computational Mechanistic Understanding to Selectivity Prediction. *Acc. Chem. Res.* **2016**, *49*, 1042−1051.

(7) Peng, Q.; Duarte, F.; Paton, R. S. Computing Organic Stereoselectivity-From Concepts to Quantitative Calculations and Predictions. *Chem. Soc. Rev.* **2016**, *45*, 6093−6107.

(8) Reid, J. P.; Sigman, M. S. Comparing Quantitative Prediction Methods for the Discovery of Small-Molecule Chiral Catalysts. *Nat. Rev. Chem.* **2018**, *2*, 290−305.

(9) Liu, D.; Xu, Z.; Yu, H.; Fu, Y. Recent DFT Calculations on the Mechanism of Transition-Metal-Catalyzed C-O Activation of Alcohols. *ChemCatChem* **2023**, *15*, No. e202300589.

(10) Rufes, A. B.; Pérez, S. P.; Poater, A. DFT in Catalysis: Complex Equations for Practical Computing Applications in Chemistry. *Digital Chem. Eng.* **2025**, No. 100285.

(11) Yang, Z.; Pan, N. Computational Studies of Ion−Neutral Reactions of Astrochemical Relevance: Formation of Hydrogen Peroxide, Acetamide, and Amino Acetonitrile. *Int. J. Mass Spectrom.* **2015**, *378*, 364−368.

(12) Vazart, F.; Calderini, D.; Puzzarini, C.; Skouteris, D.; Barone, V. State-of-the-Art Thermochemical and Kinetic Computations for Astrochemical Complex Organic Molecules: Formamide Formation in Cold Interstellar Clouds as a Case Study. *J. Chem. Theory Comput.* **2016**, *12*, 5385−5397.

(13) Kleimeier, N. F.; Eckhardt, A. K.; Kaiser, R. I. A Mechanistic Study on the Formation of Acetic Acid (CH_3COOH) in Polar Interstellar Analog Ices Exploiting Photoionization Reflectron Time-of-Flight Mass Spectrometry. *Astrophys. J.* **2020**, *901*, No. 84.

(14) Kleimeier, N. F.; Turner, A. M.; Fortenberry, R. C.; Kaiser, R. I. On the Formation of the Popcorn Flavorant 2,3-Butanedione ($CH_3COCOCH_3$) in Acetaldehyde-Containing Interstellar Ices. *ChemPhysChem* **2020**, *21*, 1531−1540.

(15) Wang, J.; Marks, J. H.; Turner, A. M.; Nikolayev, A. A.; Azyazov, V.; Mebel, A. M.; Kaiser, R. I. Mechanistical Study on the Formation of Hydroxyacetone (CH_3COCH_2OH), Methyl Acetate (CH_3COOCH_3), and 3-Hydroxypropanal ($HCOCH_2CH_2OH$) Along With Their Enol Tautomers (Prop-1-ene-1, 2-diol ($CH_3C(OH)CHOH$), Prop-2-ene-1, 2-diol ($CH_2C(OH)CH_2OH$), 1-methoxyethen-1-ol ($CH_3OC(OH)CH_2$) and Prop-1-ene-1, 3-diol ($HOCH_2CHCHOH$)) in Interstellar Ice Analogs. *Phys. Chem. Chem. Phys.* **2023**, *25*, 936−953.

(16) Fortenberry, R. C. Quantum Chemistry and Astrochemistry: A Match Made in the Heavens. *J. Phys. Chem. A* **2024**, *128*, 1555−1565.

(17) Baiano, C.; Lupi, J.; Tasinato, N.; Puzzarini, C.; Barone, V. The Role of State-of-the-Art Quantum-Chemical Calculations in Astrochemistry: Formation Route and Spectroscopy of Ethanimine as a Paradigmatic Case. *Molecules* **2020**, *25*, No. 2873.

(18) Liao, Q.; Wang, J.; Xie, P.; Liang, E.; Wang, Z. Density Functional Theory Calculations on the Interstellar Formation of Biomolecules. *Res. Astron. Astrophys.* **2023**, *23*, No. 122001.

(19) Born, M.; Oppenheimer, R. Zur Quantentheorie der Molekeln. *Ann. Phys.* **1927**, *389*, 457−484.

(20) Fukui, K. The Path of Chemical Reactions−The IRC Approach. *Acc. Chem. Res.* **1981**, *14*, 363−368.

(21) Henkelman, G.; Uberuaga, B. P.; Jónsson, H. A Climbing Image Nudged Elastic Band Method for Finding Saddle Points and Minimum Energy Paths. *J. Chem. Phys.* **2000**, *113*, 9901−9904.
(22) Trygubenko, S. A.; Wales, D. J. A Doubly Nudged Elastic Band Method for Finding Transition States. *J. Chem. Phys.* **2004**, *120*, 2082−2094.
(23) Burger, S. K.; Yang, W. Quadratic String Method for Determining the Minimum-Energy Path Based on Multiobjective Optimization. *J. Chem. Phys.* **2006**, *124*, No. 054109, DOI: 10.1063/1.2163875.
(24) E, W.; Ren, W.; Vanden-Eijnden, E. String Method for the Study of Rare Events. *Phys. Rev. B* **2002**, *66*, No. 052301.
(25) E, W.; Ren, W.; Vanden-Eijnden, E. Finite Temperature String Method for the Study of Rare Events. *J. Phys. Chem. B* **2005**, *109*, 6688−6693.
(26) Peters, B.; Heyden, A.; Bell, A. T.; Chakraborty, A. A Growing String Method for Determining Transition States: Comparison to the Nudged Elastic Band and String Methods. *J. Chem. Phys.* **2004**, *120*, 7877−7886.
(27) Quapp, W. A Growing String Method for the Reaction Pathway Defined by a Newton Trajectory. *J. Chem. Phys.* **2005**, *122*, No. 174106, DOI: 10.1063/1.1885467.
(28) Quapp, W.; Kraka, E.; Cremer, D. Finding the Transition State of Quasi-Barrierless Reactions by a Growing String Method for Newton Trajectories: Application to the Dissociation of Methylenecyclopropene and Cyclopropane. *J. Phys. Chem. A* **2007**, *111*, 11287−11293.
(29) Si, Y.; Ma, Y.; Yu, T.; Wu, Y.; Liu, Y.; Lai, W.; Zhang, Z.; Shi, J.; Guo, L.; Prezhdo, O. V.; Liu, M. Transition State Structure Detection With Machine Learnings. *npj Comput. Mater.* **2025**, *11*, No. 199.
(30) Grazioli, G.; Roy, S.; Butts, C. T. Predicting Reaction Products and Automating Reactive Trajectory Characterization in Molecular Simulations With Support Vector Machines. *J. Chem. Inf. Model.* **2019**, *59*, 2753−2764.
(31) Deringer, V. L.; Bartók, A. P.; Bernstein, N.; Wilkins, D. M.; Ceriotti, M.; Csányi, G. Gaussian Process Regression for Materials and Molecules. *Chem. Rev.* **2021**, *121*, 10073−10141.
(32) Lan, T.; An, Q. Discovering Catalytic Reaction Networks Using Deep Reinforcement Learning From First-Principles. *J. Am. Chem. Soc.* **2021**, *143*, 16804−16812.
(33) Mills, A. W.; Goings, J. J.; Beck, D.; Yang, C.; Li, X. Exploring Potential Energy Surfaces Using Reinforcement Machine Learning. *J. Chem. Inf. Model.* **2022**, *62*, 3169−3179.
(34) Barrett, R.; Westermayr, J. Reinforcement Learning for Traversing Chemical Structure Space: Optimizing Transition States and Minimum Energy Paths of Molecules. *J. Phys. Chem. Lett.* **2024**, *15*, 349−356.
(35) Kraka, E.; Antonio, J. J.; Freindorf, M. Reaction Mechanism − Explored With the Unified Reaction Valley Approach. *Chem. Commun.* **2023**, *59*, 7151−7290.
(36) Kraka, E.; Cremer, D. Computational Analysis of the Mechanism of Chemical Reactions in Terms of Reaction Phases: Hidden Intermediates and Hidden Transition States. *Acc. Chem. Res.* **2010**, *43*, 591−601.
(37) Cremer, D.; Kraka, E. From Molecular Vibrations to Bonding, Chemical Reactions, and Reaction Mechanism. *Curr. Org. Chem.* **2010**, *14*, 1524−1560.
(38) Kraka, E.; Zou, W.; Tao, Y.; Freindorf, M. Exploring the Mechanism of Catalysis with the Unified Reaction Valley Approach (URVA) - A Review. *Catalysts* **2020**, *10*, No. 691.
(39) Cremer, D.; Pople, J. A. General Definition of Ring Puckering Coordinates. *J. Am. Chem. Soc.* **1975**, *97*, 1354−1358.
(40) Fleming, K.; Kraka, E.; Computational and Theoretical Chemistry Group (CATCO). URVAvis 2026 https://github.com/SMU-CATCO/URVAvis. (Accessed May 13, 2026).
(41) Solomon, P. M.; Jefferts, K. B.; Penzias, A. A.; Wilson, R. W. Detection of Millimeter Emission Lines from Interstellar Methyl Cyanide. *Astrophys. J.* **1971**, *168*, No. L107.
(42) Hänni, N.; Altwegg, K.; Balsiger, H.; Combi, M.; Fuselier, S.; De Keyser, J.; Pestoni, B.; Rubin, M.; Wampfler, S. Cyanogen, Cyanoacetylene, and Acetonitrile in Comet 67P and Their Relation to the Cyano Radical. *Astron. Astrophys.* **2021**, *647*, No. A22.
(43) Kissel, J.; Krueger, F. The Organic Component in Dust From Comet Halley As Measured by the PUMA Mass Spectrometer on Board Vega 1. *Nature* **1987**, *326*, 755−760.
(44) Biver, N.; Bockelee-Morvan, D.; Colom, P.; Crovisier, J.; Davies, J. K.; Dent, W. R.; Despois, D.; Gerard, E.; Lellouch, E.; Rauer, H.; Moreno, R.; Paubert, G. Evolution of the Outgassing of Comet Hale-Bopp (C/1995 O1) From Radio Observations. *Science* **1997**, *275*, 1915−1918.
(45) Öberg, K. I.; Guzmán, V. V.; Furuya, K.; Qi, C.; Aikawa, Y.; Andrews, S. M.; Loomis, R.; Wilner, D. J. The Comet-Like Composition of a Protoplanetary Disk As Revealed by Complex Cyanides. *Nature* **2015**, *520*, 198−201.
(46) Bergner, J. B.; Guzmán, V. G.; Öberg, K. I.; Loomis, R. A.; Pegues, J. A Survey of CH_3CN and HC_3N in Protoplanetary Disks. *Astrophys. J.* **2018**, *857*, No. 69.
(47) Wallström, S. H. J.; Muller, S.; Roueff, E.; Le Gal, R.; Black, J.; Gérin, M. Chlorine-Bearing Molecules in Molecular Absorbers at Intermediate Redshifts. *Astron. Astrophys.* **2019**, *629*, No. A128.
(48) Muller, S.; Kawaguchi, K.; Black, J.; Amano, T. Detection of Extragalactic CF+ Toward PKS 1830−211-Chemical Differentiation in the Absorbing Gas. *Astron. Astrophys.* **2016**, *589*, No. L5.
(49) Muller, S.; Beelen, A.; Guélin, M.; Aalto, S.; Black, J. H.; Combes, F.; Curran, S.; Theule, P.; Longmore, S. Molecules at Z = 0.89-A 4-mm-Rest-Frame Absorption-Line Survey Toward PKS 1830−211. *Astron. Astrophys.* **2011**, *535*, No. A103.
(50) Krohn, O. A.; Catani, K. J.; Greenberg, J.; Sundar, S. P.; da Silva, G.; Lewandowski, H. J. Isotope-Specific Reactions of Acetonitrile (CH_3CN) With Trapped, Translationally Cold CCl^+. *J. Chem. Phys.* **2021**, *154*, No. 074305, DOI: 10.1063/5.0038113.
(51) Herbst, E.; Van Dishoeck, E. F. Complex organic interstellar molecules. *Annu. Rev. Astron. Astrophys.* **2009**, *47*, 427−480.
(52) Ceccarelli, C.; Caselli, P.; Fontani, F.; Neri, R.; López-Sepulcre, A.; Codella, C.; Feng, S.; Jiménez-Serra, I.; Lefloch, B.; Pineda, J. E.; Vastel, C.; Alves, F.; Bachiller, R.; Balucani, N.; Bianchi, E.; Bizzocchi, L.; Bottinelli, S.; Caux, E.; Chacón-Tanarro, A.; Choudhury, R.; Coutens, A.; Dulieu, F.; Favre, C.; Hily-Blant, P.; Holdship, J.; Kahane, C.; Al-Edhari, A. J.; Laas, J.; Ospina, J.; Oya, Y.; Podio, L.; Pon, A.; Punanova, A.; Quenard, D.; Rimola, A.; Sakai, N.; Sims, I. R.; Spezzano, S.; Taquet, V.; Testi, L.; Theulé, P.; Ugliengo, P.; Vasyunin, A. I.; Viti, S.; Wiesenfeld, L.; Yamamoto, S. Seeds Of Life In Space (SOLIS): The Organic Composition Diversity at 3001000 au Scale in Solar-type Star-forming Regions. *Astrophys. J.* **2017**, *850*, No. 176.
(53) Pentsak, E. O.; Murga, M. S.; Ananikov, V. P. Role of acetylene in the chemical evolution of carbon complexity. *ACS Earth Space Chem.* **2024**, *8*, 798−856.
(54) Ruiz-Mirazo, K.; Briones, C.; de la Escosura, A. Prebiotic systems chemistry: new perspectives for the origins of life. *Chem. Rev.* **2014**, *114*, 285−366.
(55) Sandford, S. A.; Nuevo, M.; Bera, P. P.; Lee, T. J. Prebiotic astrochemistry and the formation of molecules of astrobiological interest in interstellar clouds and protostellar disks. *Chem. Rev.* **2020**, *120*, 4616−4659.
(56) Fleming, K.; Kraka, E. Examining Interstellar Ion-Neutral Reactions Using the Unified Reaction Valley Approach: The Case of the $CCl^+ + CH_3CN$ Reaction. *ACS Earth Space Chem.* **2025**, *9*, 1837−1847.
(57) Riplinger, C.; Neese, F. An Efficient and Near Linear Scaling Pair Natural Orbital Based Local Coupled Cluster Method. *J. Chem. Phys.* **2013**, *138*, No. 034106, DOI: 10.1063/1.4773581.
(58) Kendall, R. A.; Dunning, T. H.; Harrison, R. J. Electron Affinities of the First-Row Atoms Revisited. Systematic Basis Sets and Wave Functions. *J. Chem. Phys.* **1992**, *96*, 6796−6806.
(59) Woon, D. E.; Dunning, T. H. Gaussian Basis Sets for Use in Correlated Molecular Calculations. III. The Atoms Aluminum Through Argon. *J. Chem. Phys.* **1993**, *98*, 1358−1371.
(60) Head-Gordon, M.; Pople, J. A.; Frisch, M. J. MP2 Energy Evaluation by Direct Methods. *Chem. Phys. Lett.* **1988**, *153*, 503−506.

(61) Dunning, T. H. Gaussian Basis Sets for Use in Correlated Molecular Calculations. I. The Atoms Boron Through Neon and Hydrogen. *J. Chem. Phys.* **1989**, *90*, 1007−1023.
(62) Lee, T. J.; Schaefer, H. F., III The Classical and Nonclassical Forms of Protonated Acetylene, $C_2H_3^+$. Structures, Vibrational Frequencies, and Infrared Intensities From Explicitly Correlated Wave Functions. *J. Chem. Phys.* **1986**, *85*, 3437−3443.
(63) Lindh, R.; Roos, B. O.; Kraemer, W. P. A CAS SCF CI Study of the Hydrogen Migration Potential in Protonated Acetylene, $C_2H_3^+$. *Chem. Phys. Lett.* **1987**, *139*, 407−416.
(64) Lindh, R.; Rice, J. E.; Lee, T. J. The Energy Separation Between the Classical and Nonclassical Isomers of Protonated Acetylene. An Extensive Study in One−and N-Particle Space. *J. Chem. Phys.* **1991**, *94*, 8008−8014.
(65) Curtiss, L. A.; Pople, J. A. Theoretical Study of Structures and Energies of Acetylene, Ethylene, and Vinyl Radical and Cation. *J. Chem. Phys.* **1988**, *88*, 7405−7409.
(66) Psciuk, B. T.; Benderskii, V. A.; Schlegel, H. B. Protonated Acetylene Revisited. *Theor. Chem. Acc.* **2007**, *118*, 75−80.
(67) Sharma, A. R.; Wu, J.; Braams, B. J.; Carter, S.; Schneider, R.; Shepler, B.; Bowman, J. M. Potential Energy Surface and MULTI-MODE Vibrational Analysis of $C_2H_3^+$. *J. Chem. Phys.* **2006**, *125*, No. 224306, DOI: 10.1063/1.2402169.
(68) Crofton, M. W.; Jagod, M.-F.; Rehfuss, B. D.; Oka, T. Infrared Spectroscopy of Carbo-Ions. V. Classical vs Nonclassical Structure of Protonated Acetylene $C_2H_3^+$. *J. Chem. Phys.* **1989**, *91*, 5139−5153.
(69) Gabrys, C. M.; Uy, D.; Jagod, M.-F.; Oka, T.; Amano, T. Infrared Spectroscopy of Carboions. 8. Hollow Cathode Spectroscopy of Protonated Acetylene, $C_2H_3^+$. *J. Phys. Chem. A* **1995**, *99*, 15611−15623.
(70) Knoll, L.; Vager, Z.; Marx, D. Experimental Versus Simulated Coulomb-Explosion Images of Flexible Molecules: Structure of Protonated Acetylene $C_2H_3^+$. *Phys. Rev. A* **2003**, *67*, No. 022506.
(71) Vager, Z.; Zajfman, D.; Graber, T.; Kanter, E. Experimental Evidence for Anomalous Nuclear Delocalization in $C_2H_3^+$. *Phys. Rev. Lett.* **1993**, *71*, No. 4319.
(72) Kalescky, R.; Santos, C. V., Jr.; Tao, Y.; Zou, W.; Freindorf, M.; Cremer, D.; Kraka, E.; Computational and Theoretical Chemistry Group (CATCO). *URVA 2025*; Southern Methodist University: Dallas, TX, USA, 2025.
(73) Computational and Theoretical Chemistry Group (CATCO). SMU-CATCO GitHub 2026 https://github.com/SMU-CATCO. (Accessed May 29, 2026).
(74) Hratchian, H. P.; Kraka, E. Improved Predictor-Corrector Integrators For Evaluating Reaction Path Curvature. *J. Chem. Theory Comput.* **2013**, *9*, 1481−1488.
(75) Bahn, S. R.; Jacobsen, K. W. An Object-Oriented Scripting Interface to a Legacy Electronic Structure Code. *Comput. Sci. Eng.* **2002**, *4*, 56−66.
(76) Larsen, A. H.; Mortensen, J. J.; Blomqvist, J.; Castelli, I. E.; Christensen, R.; Dułak, M.; Friis, J.; Groves, M. N.; Hammer, B.; Hargus, C.; Hermes, E. D.; Jennings, P. C.; Jensen, P. B.; Kermode, J.; Kitchin, J. R.; Kolsbjerg, E. L.; Kubal, J.; Kaasbjerg, K.; Lysgaard, S.; Maronsson, J. B.; Maxson, T.; Olsen, T.; Pastewka, L.; Peterson, A.; Rostgaard, C.; Schiøtz, J.; Schütt, O.; Strange, M.; Thygesen, K. S.; Vegge, T.; Vilhelmsen, L.; Walter, M.; Zeng, Z.; Jacobsen, K. W. The Atomic Simulation Environment—A Python Library for Working With Atoms. *J. Phys.:Condens. Matter* **2017**, *29*, No. 273002.
(77) Glendening, E. D.; Badenhoop, J. K.; Reed, A. E.; Carpenter, J. E.; Bohmann, J. A.; Morales, C. M.; Karafiloglou, P.; Landis, C. R.; Weinhold, F. *NBO 7.0*; University of Wisconsin: Madison, 2018.
(78) Glendening, E. D.; Landis, C. R.; Weinhold, F. NBO 7.0: New Vistas in Localized and Delocalized Chemical Bonding Theory. *J. Comput. Chem.* **2019**, *40*, 2234−2241.
(79) Bader, R. F. W. A Quantum Theory of Molecular Structure and Its Applications. *Chem. Rev.* **1991**, *91*, 893−928.
(80) Oliveira, V.; Kraka, E.; Cremer, D. The Intrinsic Strength of the Halogen Bond: Electrostatic and Covalent Contributions Described by Coupled Cluster Theory. *Phys. Chem. Chem. Phys.* **2016**, *18*, 33031−33046.
(81) Pak, Y.; Woods, R. C. Spectroscopic constants and potential energy functions of OCCl+, ONP, ONS+, ArCN+, OCS, and NCCl using the coupled cluster method. *J. Chem. Phys.* **1997**, *107*, 5094−5102.